Magnetic Resonance Imaging 60 (2019) 130–136

Contents lists available at ScienceDirect

Magnetic Resonance Imaging

journal homepage: www.elsevier.com/locate/mri

Original contribution

Accelerated positive contrast MRI of interventional devices using parallel compressed sensing imaging

Samira Vafay Eslahi, Jim Ji*

Department of Electrical and Computer Engineering, Texas A&M University, College Station, TX, USA

ARTICLE INFO

Keywords:
Positive contrast MRI
Interventional imaging
Parallel MRI
Susceptibility mapping

ABSTRACT

Susceptibility-based magnetic resonance imaging (MRI) method can image small MR-compatible devices with positive contrast. However, the relatively long data acquisition time required by the method hinders its practical applications. This study presents a parallel compressive sensing technique with a modified fast spin echo to accelerate data acquisition for the susceptibility-based positive contrast MRI. The method integrates the generalized autocalibrating partially parallel acquisitions and the compressive sensing techniques in the reconstruction algorithm. MR imaging data acquired from several phantoms containing interventional devices such as biopsy needles, stent, and brachytherapy seeds, used for validating the proposed technique. The results show that it can speed up data acquisition by a factor of about five while preserving the quality of the positive contrast images.

1. Introduction

Success in image-guided therapy relies on accurate localization of both the treatment targets and interventional devices [1,2]; imaging plays a significant role in this aim. Although magnetic resonance imaging (MRI) is a prime imaging method in both diagnosis and target definition [3–5], its application in guiding the interventional procedure or localizing devices is very limited. This limitation is largely attributable to signal loss due to the high susceptibility of the devices and, consequently, to the appearance of black voids in the immediate vicinity of the interventional devices [6–8]. In MR images, these black voids prevent the devices from being differentiated from other dark features of the tissues, such as arteries or natural cavities [9–11]. A susceptibility-based MRI method is available that can visualize small MR compatible devices and can reduce the signal loss using a fast spin-echo sequence [12–15]; however, data acquisition with this method still takes about 10 (or more) minutes, which hinders its clinical application.

Many methods have been developed to accelerate data acquisition in clinical MRI. Two important ones are parallel magnetic resonance imaging (pMRI) [16] and compressive sensing (CS) [17–21]. The pMRI technique can shorten the scan time by taking advantage of the complementary channel sensitivities of the multiple receivers to reduce the amount of data needed to reconstruct an image. Different methods of pMRI have been proposed to reconstruct the image with undersampled k-space data to reduce the artifacts and noise [22–25]; however, the undersampling factor in pMRI is limited. CS can also reduce the amount of data needed for MRI reconstruction if the sparsity (compressibility under certain transformations) and the encoding incoherency are satisfied [19]. CS reconstructs the image from the undersampled k-space data using the ℓ_1 minimization technique [19]. The combination of pMRI and CS has also been introduced in MRI applications, which significantly improved the quality of the image as compared to pMRI and CS alone [26–31].

In the present study, we propose to integrate the generalized autocalibrating partially parallel acquisitions (GRAPPA) technique [23,32,33] and the CS modality to accelerate data acquisition for positive contrast MRI of interventional devices. The method reconstructs images from the undersampled k-space data and preserves the phase information for susceptibility mapping. In the phantom studies, up to five acceleration factors were feasible. When used with the fast spin-echo sequence method, the proposed method can achieve an order of magnitude speed-up comparable to the other spin-echo sequence acquisitions. This makes it more suitable for clinical applications to localize small metallic devices. A preliminary version of this study has been reported in [34,35].

* Corresponding author.
E-mail address: jimji@tamu.edu (J. Ji).

https://doi.org/10.1016/j.mri.2019.04.006
Received 5 December 2018; Received in revised form 4 April 2019; Accepted 6 April 2019

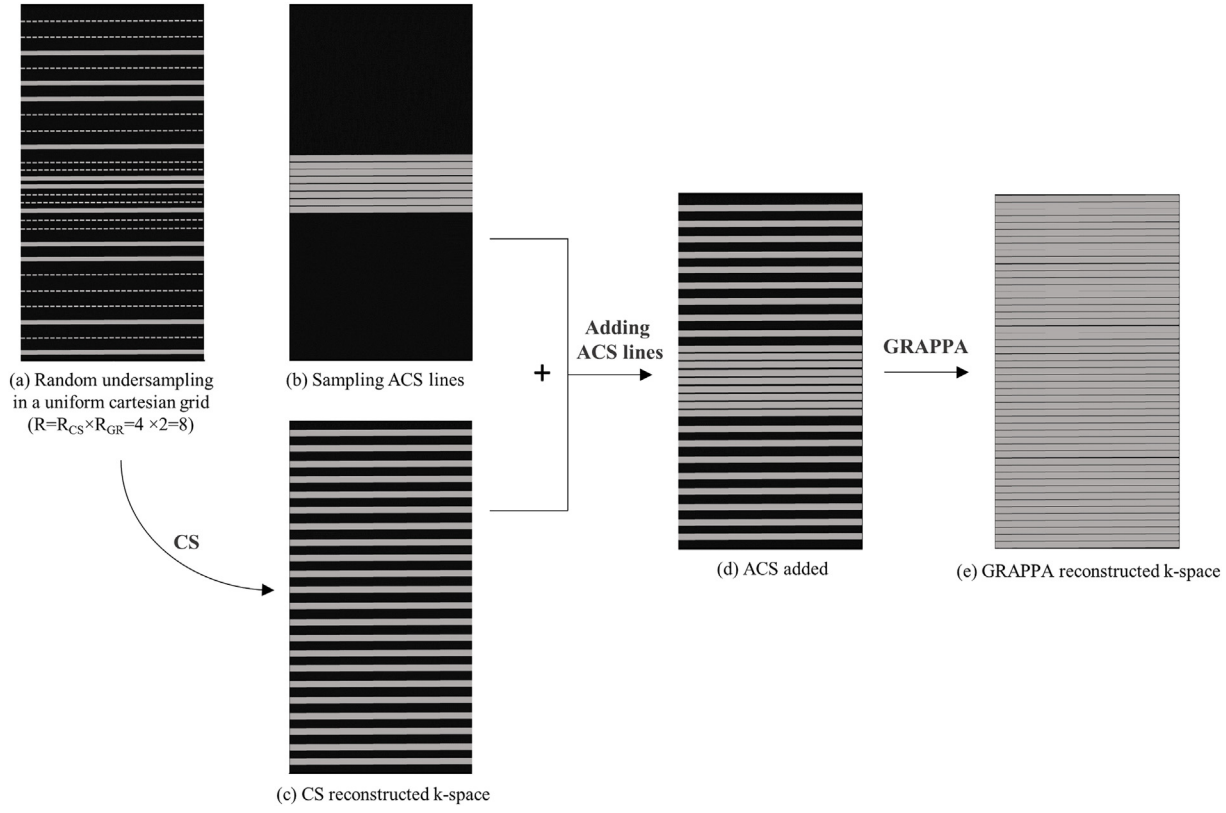

Fig. 1. The procedure of undersampling the k-space data with a reduction factor of eight in the proposed method. The data are randomly sampled (for CS) on a uniformly undersampled k-space (for GRAPPA). Random variable density sampling is used for CS and full sampling is used for ACS lines. Then, CS will reconstruct the randomly sampled data and the generated k-space will be the input for GRAPPA. Finally, by adding the ACS lines, GRAPPA will reconstruct the full k-space.

2. Materials and methods

2.1. Data acquisition and image reconstruction

The data acquisition scheme is shown in Fig. 1. To preserve the phase in the reconstructed images, the data acquisition consists of two parts of k-space: a) randomly undersampled outer part of the k-space, shown in Fig. 1.a, and b) fully sampled auto-calibration signals (ACS) shown in Fig. 1.b. In the regular random sampling, some lines in k-space will be selected randomly, but as the ACS lines at the center of the k-space have the highest energy and the most important contrast information, variable density random sampling has been applied to keep the center denser. The data sampling pattern in part b is to provide the ACS needed for GRAPPA reconstruction and consequently for the proposed method. Fully sampled Central ACS lines also contribute to the variable density random sampling data needed for CS reconstruction.

Data sampling in Fig. 1.a has a special pattern. The data are randomly sampled at a specific undersampling factor (R_{CS}) on a fixed uniform grid corresponding to a reduced field-of-view (FOV). The size of the reduced FOV is determined by a GRAPPA reduction factor (R_{GRAPPA}). Therefore, the total k-space undersampling reduction factor (R) is $R = R_{CS} \times R_{GRAPPA}$. The actual reduction factor in data acquisition will be determined by the total acquisition lines in (a)∪(b) as compared to the total k-space data sampled for the full FOV.

The random variable density undersampling scheme has several advantages. It keeps the center lines of the k-space data which have the highest energy and thus helps to minimize the artifacts in the reconstruction. Also, for CS reconstruction, random undersampling leads to incoherency with respect to the sparsifying transform. It spreads the artifacts over the FOV image and by ℓ_1 norm minimization reduces or even eliminates them. For GRAPPA reconstruction, the data acquisition provides ACS as well as uniform undersampling data after the CS reconstruction step.

The image reconstruction has two main steps: 1) CS reconstruction of a reduced FOV image from each channel, and 2) GRAPPA reconstruction of a full FOV image from each channel. The two-step reconstruction takes advantage of the complementary redundancies in image sparsity and coil sensitivity. More importantly, it preserves the image phase in each step, which is critical for field mapping and susceptibility calculation. For step 1, data recovery (as shown in Fig. 1.c) from each channel can be modeled as,

$$d_l = SFI_l = \phi I_l \tag{1}$$

where d_l is the randomly acquired k-space data in the uniform grid, l is the channel index, I_l is each channel's image, and ϕ is the combination of the Fourier transformation F and undersampling operator S. Based on the CS theory each channel image can be reconstructed by [19],

$$\begin{aligned} &\underset{I_l}{\text{minimize}} \quad TV(I_l) \\ &\text{subject to} \quad \|\phi I_l - d_l\|_2 < \epsilon \end{aligned} \tag{2}$$

TV is the total variation, which reflects the sum of the absolute variations in the image. TV is defined as $\Sigma_p |D_p I_l|$, where $D_p I_l$ represents the horizontal and vertical finite differences of I_l at pixel p in the whole image [20,36,37]. The parameter ϵ is a small number determined by the data noise level. An iterative algorithm can be used to solve Eq. (2). Note the outcome I_l is a reduced FOV image. After CS reconstruction, in step 2, GRAPPA is used to reconstruct a full FOV complex image for each channel. GRAPPA uses ACS lines and multiple block-wise interpolations to recover the missing lines. In step 2, the missing line $(k_y - m\Delta k_y)$ offset from the normally acquired data in the coil j, will be recovered [23] by,

$$S_j(k_y - m\Delta k_y) = \sum_{l=1}^{L} \sum_{b=0}^{N_b-1} n(j,b,l,m) S_l(k_y - bR_{GR}\Delta k_y) \tag{3}$$

where l counts the coils, L is the total number of channels, b counts the blocks, N_b is the total number of blocks (each block is defined as a single acquired line and $R_{GR} - 1$ missing lines), $n(j,b,l,m)$ represent the weighting factor to produce sinusoidal spatial sensitivity profile with the harmonies of order m, and $\Delta k_y = 2\pi/FOV$ is the minimum k-space interval related to the reduced FOV [24]. When all the missing lines have been recovered, a full FOV channel image ($\hat{I}^l$) can be simply reconstructed by Fourier transform for each channel.

2.2. Positive contrast image reconstruction

The positive contrast image is reconstructed following the procedure in [13]. Specifically, when all the channel images are reconstructed, a combined magnitude image is produced by the sum of squares (SOS) reconstruction. Then, a combined phase image is extracted from the weighted average of all the complex images of all the channels.

$$\hat{I} = \left(\sum_{l=1}^{L} | \hat{I}^l | e^{j\theta^l_{diff}} \right) / L \tag{4}$$

Here we define $\theta^l_{diff} = \angle \hat{I}_{2l} \cdot \hat{I}^*_{1l}$, in which $\hat{I}_{2l}$ and $\hat{I}^*_{1l}$ are the image and conjugate image acquired from the sequences with and without echo shifts in the l^{th} channel, respectively.

Then, the positive contrast images can be generated by the susceptibility mapping using the combined magnitude and phase images. In a modified fast spin-echo sequence, the local field variation calculation differs from the conventional SE-based technique, in which two images are acquired based on shifting the 180-degree refocusing pulse of one of the sequences toward the 90-degree refocusing pulse in the amount of T_{shift} equals to 0.6 ms. The local field variation can be generated based on the magnetic susceptibility of the inserted object. The object inside the tissue generates an inhomogeneous local magnetic field, whereby two different images will be generated by acquiring two sets of data with different local magnetic fields. The local magnetic field difference can be calculated by [12],

$$\Delta B = \theta_{diff} / (2\gamma B_0 \Delta T_{shift}) \tag{5}$$

where θ_{diff} is the combined phase differences calculated from Eq. (4), γ is the gyromagnetic ratio, B_0 is the static magnetic field, and ΔT_{shift} is the echo shift between two acquisitions. The susceptibility map can be reconstructed based on the calculated local field by solving the ℓ_1 norm minimization problem [38–40]:

$$argmin_{\chi} \ \| W(C\chi - \Delta B) \|_2^2 + \lambda \ \| MG\chi \|_1 \tag{6}$$

where χ is the susceptibility map, W is the weighting matrix derived from the normalized magnitude image, C is the dipole kernel convolution operator, λ is a regularization parameter, M is the mask that identifies the area of low signal intensities and potential location of devices, and G is the three-dimensional gradient operator to calculate the susceptibility gradient. This procedure makes it possible to have reliable reconstruction even at areas of low signal intensities and rapid phase mapping [13]. Fig. 2 shows the proposed reconstruction procedure.

2.3. Experiment and simulation

The experiments were performed on three different phantoms to validate the proposed method. The dataset was acquired on a 3 Tesla whole-body scanner (Siemens AG, Erlangen, Germany) using eight channel coils and the modified fast spin-echo sequence. Two datasets were obtained for each phantom, one with no echo shift and the other with echo shift (T_{shift}= 0.6 ms). The turbo factor considered in the acquisitions is 7.

The phantom for the first experiment was constructed by inserting a biopsy needle into a bottle of water. The biopsy needle was made of titanium, was 160 mm long and 2 mm in diameter. The phantom was constructed by filling a sealed plastic container with distilled water doped with 1.0 gl^{-1} copper sulfate solution. The needle was positioned parallel to the magnetic field. Forty-two axial slices were acquired. Scan parameters were FOV = 80 mm × 80 mm × 80 mm, matrix size = 132 × 128 × 42, TR = 2000 ms, TE = 18 ms, in-plane resolution = 0.625 mm × 0.625 mm, slice thickness = 1.5 mm, slice gap = 25%, bandwidth = 134 Hz/Pixel, T_{shift} = 0.6 ms (with echo shift) and 0 ms (without echo shift). The total acquisition time was 4 min.

The second experiment was performed using a phantom containing a tracheal stent (manufactured by Micro-Tech, Nanjing Co., Ltd). The acquisition was done by inserting a stent in some gelatin phantom doped with 1.0 g/l copper sulfate solution. The stent was made of Ni−Ti alloy with magnetic susceptibility, $\chi_{nitinol}$ of 245 ppm, 60 mm in length, 20 mm in diameter, and the wire had a diameter of 0.24 mm. The axis of the stent was oriented perpendicular to the direction of the magnetic field. Scan parameters were: FOV = 95 mm× 95 mm, voxel size = 0.367 mm × 0.371 mm × 1.5 mm, matrix size = 259 × 256 × 17, TR = 2000 ms, TE = 18 ms, in-plane resolution = 0.37 mm× 0.37 mm, slice thickness = 1.5 mm, no slice gap, bandwidth = 134 Hz/Pixel, and T_{shift} = 0.6 ms.

In the third experiment, data were acquired by inserting five dummy brachytherapy seeds in porcine tissue with different spacing. Each seed is a silver rod impregnated with iodine-125 enclosed in a titanium capsule with hemispherical ends. A plastic stick, a bamboo toothpick, and a small animal bone were also inserted in the tissue to simulate a cavity, a capillary, and a human bone, respectively. The placement of seeds was done such that their orientations are along the B_0 filed. Acquisition of image slices was done along the coronal plane, while the seeds were oriented along the longitudinal direction. A modified fast spin-echo sequence was used to acquire the data with scan parameters as follows: FOV = 120 mm× 120 mm × 15 mm, matrix size = 192 × 192 × 10, TR = 2000 ms, TE = 18 ms, in-plane resolution = 0.625 mm× 0.625 mm, slice thickness = 1.5 mm, no slice gap, and bandwidth = 134 Hz/Pixel. The total acquisition time was 3.9 min. The undersampled data acquisitions in Fig. 1 were simulated by decimating the fully sampled datasets. This allows comparison with the conventional reconstruction techniques.

There is a trade-off between the error and the scan time in choosing the number of ACS lines. The number of ACS lines assigned to the center for sampling was tested and the best result chosen. In addition, GRAPPA uses a defined number of blocks to select the neighbor lines of any of the ACS lines to calculate the missing lines with the closest high-energy signals and with the most significant information. Increasing the number of blocks can fit each of the missing lines with more information; however, increasing the number of blocks can increase the computation time. In this case, the most efficient number of blocks is chosen among all other tested results, which is two blocks in each calibrating iteration. The same procedure was used to choose the optimal number of columns. Three-dimensional views of the contrast images of the devices were generated using the method of maximum intensity projection (MIP).

Quantitative evaluation of the intensity in the positive contrast images was measured by the half-intensity region (HIR) technique [13]. HIR measures the number of pixels that have more intensities than the background by at least,

$$\frac{1}{2}(\chi_{max} - \chi_{min}) \tag{7}$$

where χ_{max} is the maximum and $\chi_{min}$is the minimum intensity of the positive contrast images. The mean and the standard deviation of all the numbers of pixels above the threshold are calculated for HIR evaluation. On the other hand, the image reconstruction error is calculated by the artifact power (AP) technique based on the reference by,

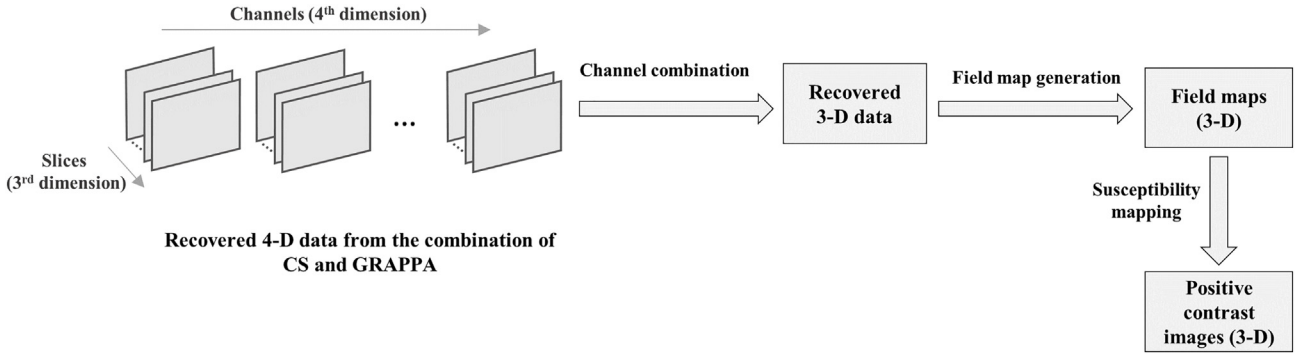

Fig. 2. Positive contrast image reconstruction with the proposed method. The images of the combined channels are used for field map calculation. The dimension is reduced to three in this stage as the channels are combined. Ultimately, the positive contrast images are reconstructed for all of the slices. The difference between the proposed method, CS-alone and GRAPPA-alone, is the reconstruction procedure of each of the slices. The Channel combination and other steps will remain virtually unchanged.

$$AP = \sqrt{\frac{\sum_{z=1}^{N_z}\sum_{y=1}^{N_y}\sum_{x=1}^{N_x}(\chi_{xyz} - \chi_{xyz}^{ref})^2}{N_z \times N_y \times N_x}} \quad (8)$$

where χ_{xyz} is the positive image of the recovered data, χ_{xyz}^{ref} is the positive contrast image of the reference, N_x is the total number of frequency encoding lines, N_y is the total number of phase encoding lines, and N_z is the total number of slices.

The other evaluation was done by measuring the signal-to-noise ratio (SNR). The SNR was calculated by defining a region around the needle in the SOS of the positive contrast images as a signal and a defined region in the background as noise.

The simulation was done by a MATLAB R2016a software. All simulations were performed on a workstation of Intel (R) Core (TM) i7, 4700HQ CPU, 64-bit processor, and 12 GB memory. In addition, the PULSAR toolbox is used to simulate the GRAPPA reconstruction [41].

3. Results

The results for the first experiment are shown in Fig. 3. The first two rows show the reconstructed MR magnitude and phase images, and the next two rows show the corresponding, combined images. The large black void surrounding the needle is due to the susceptibility artifact and signal loss. The positive contrast images from susceptibility mapping, and the corresponding MIP renderings using all slices are shown on the last two rows, respectively. The reconstruction used the full FOV k-space data is used as the reference image. In addition, CS-alone and GRAPPA-alone reconstructions are compared with the proposed method with reduction factors of $R = 2 \times 4$ and $R = 4 \times 2$. The positive contrast image with 8-fold acceleration has shown that it is comparable to the reference image, and clearly shows the position of the needle in the phantom. The results in Fig. 3 show that the proposed method with $R = 4 \times 2$ yields the highest quality in positive contrast and MIP images. In addition, the intensity of the needle is closer to that on the reference.

Quantitative comparison of the different methods in the first experiment is shown in Table 1. It is clearly shown that the HIR of the proposed method (with $R = 4 \times 2$) is closer to the reference compared with the other methods. This means that the proposed method has the highest accuracy of the compared methods. Although the AP remains approximately the same in all methods, the SNR and HIR of the proposed method are generally superior to the others, although the proposed method is slightly slower than CS. This means that the proposed acceleration method can localize and visualize the interventional devices, even when its scanning is five times faster than the reference with fully sampled k-space data. Qualitative and quantitative Results with different reduction factor combinations shows that they should be carefully chosen to achieve optimal image quality.

As shown in Fig. 3 and Table 1, the SNR in CS-alone reconstruction is generally higher than that of the GRAPPA-alone reconstruction. The GRAPPA-alone reconstructions, on the other hand, show higher resolution, less blurring, but more artifacts than the CS-alone reconstruction. The local phase of the proposed method is closer to that of the reference, which demonstrates the superiority of the proposed method. Although not all channel and slice images are shown in the paper due to the space limit, this is observed in the individual slice images and the combined images. The proposed method provides a trade-off, when high acceleration factors are used, between the high SNR of the CS reconstructions and high resolution in GRAPPA reconstructions. A general observation, as expected, is that the reduction factors for the CS and GRAPPA steps can be adjusted to make the final reconstruction be closer to either the CS or the GRAPPA reconstruction.

The results for the second experiment are shown in Fig. 4. The proposed method used on the stent data with reduction factor 8, shows acceptable visualization of the mesh. The MIP shows that the stent is localized, as is the reference. The magnitude images are slightly blurred due to the CS reconstruction, making it difficult to accurately localize the stent data. However, the susceptibility mapping method clearly visualizes the stent data. The proposed method decreases the scan time while showing the exact location of the stent data. The MIP views of the stent implanted in the phantom show all the slices in their exact location and also show the helical structure with the exact dimension, as compared to the reference. In addition, it is clear that the positive contrast image of the stent has the highest quality as compared to the GRAPPA alone or CS alone.

The results for the third experiment are shown in Fig. 5. Five dummy brachytherapy seeds were inserted in porcine tissue with different spacing, one time with random sampling and the other time the full k-space was scanned for comparison. The MIP shows that the proposed method has the highest seed intensity and highest SNR in comparison to the reference, rather than CS alone and GRAPPA alone and the seeds are clearly shown. Therefore, the proposed method works well with seed data as well.

4. Discussion

The proposed method was introduced to accelerate data acquisition for positive contrast MRI to visualize and localize interventional devices at an acceleration factor of up to 5. Although CS-GRAPPA has previously been shown in fMRI and other MRI applications, only the magnitude images were used. In the proposed method, phase information is presented in the reconstruction and is used for susceptibility mapping. The noise and artifact power were decreased as compared to the GRAPPA or CS reconstructions alone.

The aim of this study was to reduce the scan time, which plays a

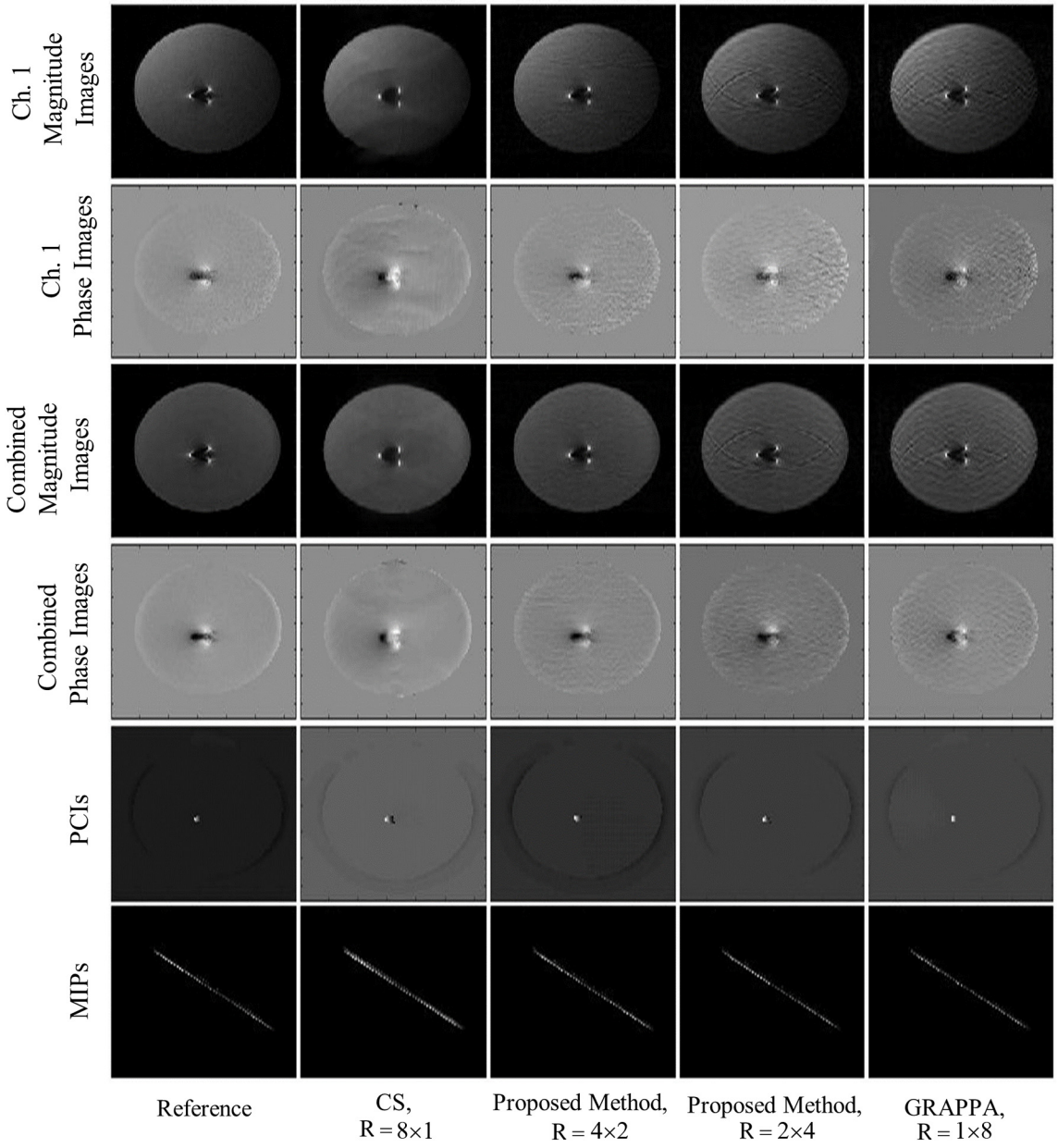

Fig. 3. The first and third rows show the magnitude images of the first and the combined channels with different methods; second and fourth rows are the corresponding phase images; fifth and the last row are the PCI and MIP views of the positive contrast images and all with $R = 8$ ($\mathbf{R}_{CS} \times \mathbf{R}_{GRAPPA}$). The phase image will be as important as the magnitude image in PCI calculation and the proposed method has the best phase image. Therefore, the proposed method has the best PCI compared to the other methods.

Table 1
Comparison of the proposed methods, HIR (mean ± SD), AP (Artifact power), SNR, and the actual scan time (minutes) with the reference, CS, proposed method with $R = 4 \times 2$, proposed method with $R = 2 \times 4$, and GRAPPA in a phantom with an inserted biopsy needle. Here, R stands for the combined reduction factor ($\boldsymbol{R}_{CSGRAPPA}$) that the first number shows CS and the second shows GRAPPA reduction factors.

Method of reconstruction	HIR	AP × 10^{-7}	SNR × 10^{4}	Scan time
Reference	2.02 ± 1.38	–	1.63	4
CS	2.34 ± 0.92	1.22	5.74	0.51
Proposed method, R = 4 × 2	1.94 ± 0.91	1.09	2.43	0.58
Proposed method, R = 2 × 4	1.80 ± 1.14	0.63	1.19	0.74
GRAPPA	1.54 ± 1.08	0.96	1.08	1.04

significant role in MRI applications. The results show that the interventional devices could be clearly visualized in positive contrast images by applying the proposed method; moreover, the image quality is comparable to the reference, while the scan time is decreased by up to 5 times. However, a combination of the CS and GRAPPA can increase the computation time, as compared to CS alone or to GRAPPA alone. This is for the reason of containing both steps of CS and GRAPPA at the same time. Increasing the iteration number in CS may increase the quality, but also increases the computation time. To address this issue, future work will investigate simplified non-iterative positive contrast reconstruction methods or parallel computing. Although CS uses an iterative algorithm, the computation time is shorter than GRAPPA in our studies. We believe that it is because GRAPPA uses a 4D kernel including all channels and a large neighborhood in the 3D k-space. It is possible to reduce this computation by using the channel reduction method and smaller kernels [42].

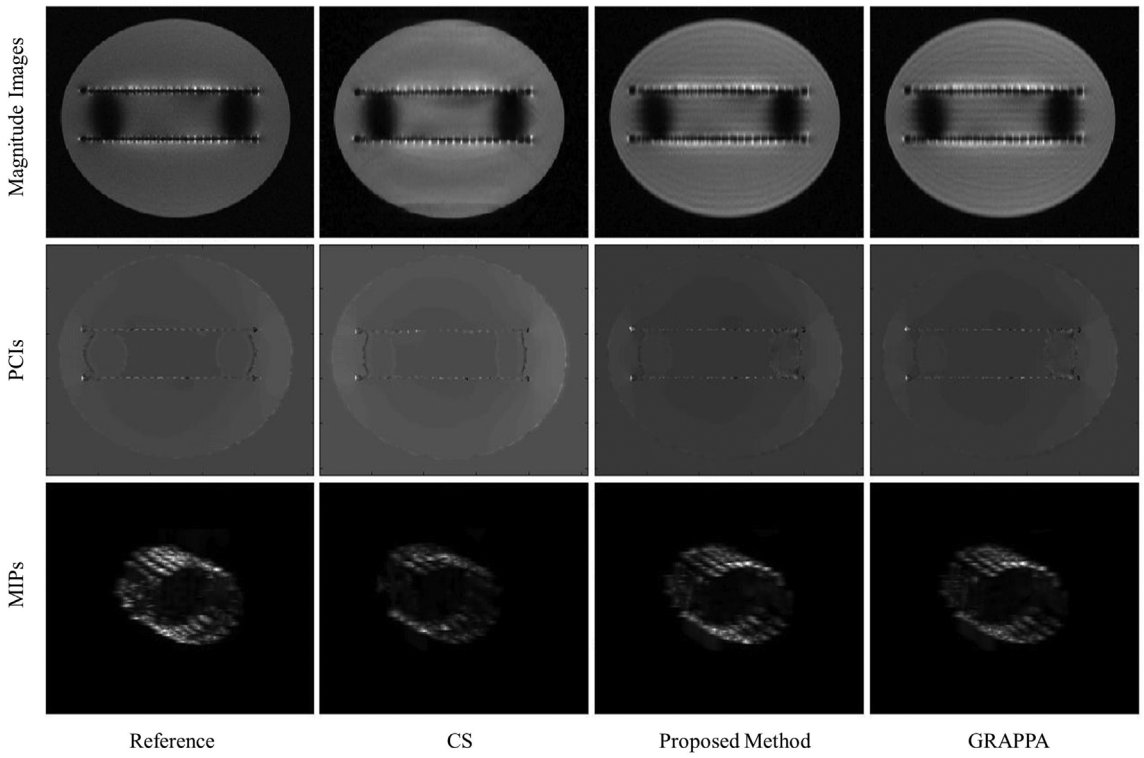

Fig. 4. Evaluation of the proposed method on stent data. The first row shows the magnitude images, the second row the SOS of the positive contrast images of all the channels, third row contains the MIP generated from positive contrast images from all the slices; all the methods are with $R = 8$. In magnitude images, CS is showing a smoother image compared to others, but it is blurry and the phase will not be as well as the proposed method. Second and third row show the proposed method can visualize and localize the mesh with high intensity and closer to the reference.

In visualizing the interventional device, both the quality of the positive contrast images and the localization of the devices are important. Other highly susceptible objects may also be shown in the positive contrast images. However, early work has shown that biologically relevant objects (such as bones or blood) have much lower susceptibility than interventional devices and usually will not create false position problems [13]. In addition, positive contrast device images can be combined with magnitude MR images to show pathology

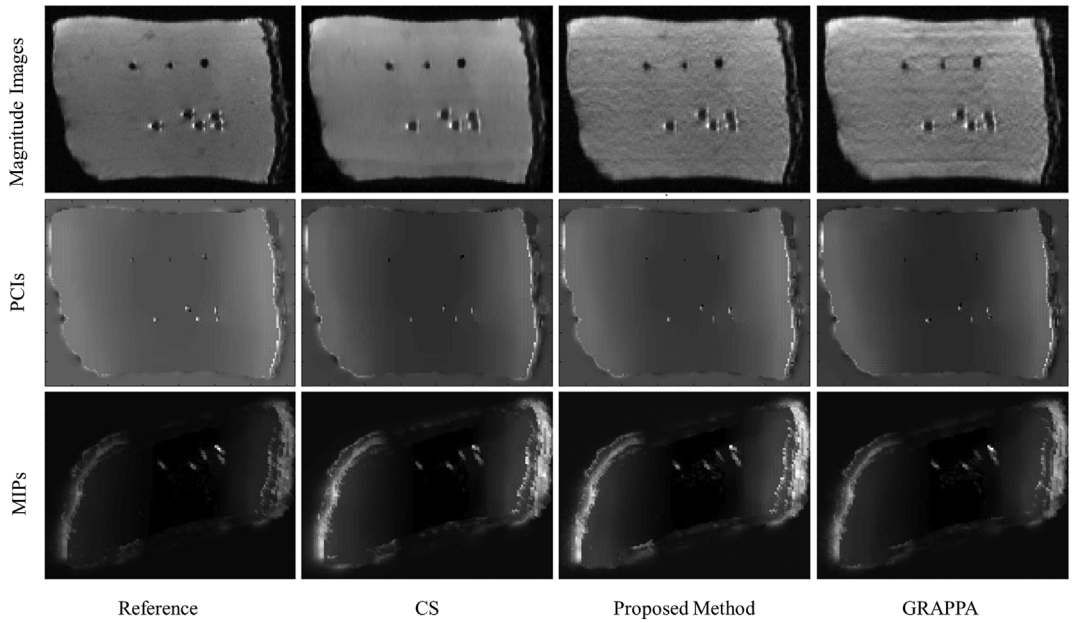

Fig. 5. Evaluation of the proposed method for brachytherapy seed data. First row: Magnitude images, Second row: positive contrast images, and third row: MIP generated images. The other data used for evaluation are the seed data and all are undersampled with $R = 8$. Although in the first row CS is showing very smooth and clear magnitude image with less artifact compared to other methods, the PCI in CS is very blurry and the proposed method has the best PCI compared to the other two methods. Applying the proposed method on these data confirms that the proposed method can visualize and localize the seeds by preserving the exact locations of the seeds with a higher intensity than those of the other two methods.

and anatomical objects. Finally, the present study is limited to phantom experiments and simulations; additional studies are needed to validate the proposed method for clinical applications.

5. Conclusions

This study has proposed an accelerated positive contrast imaging method with an integrated reconstruction technique for visualizing interventional devices. Integrating CS and GRAPPA improved the image quality and preserved the phase for the reconstruction of the positive contrast images. This method can reduce the scan time in phantom studies by a factor of five and still provides images to visualize and localize the devices with high accuracy. As compared to reconstructions based on the CS method alone and the GRAPPA method alone, in all the experiments the proposed method provided improved visualization and localization. Therefore, the proposed accelerated method has the potential to reduce the scan time significantly in clinical applications of positive-contrast MRI methods.

Acknowledgment

Funding: This work was partially supported by the National Science Foundation under grant number 1606136. Any opinions, findings and conclusions or recommendations expressed in this material are those of the authors and do not necessarily reflect those of the National Science Foundation.

The authors would like to acknowledge Ms. Caiyun Shi and Dr. Guoxi Xie for their assistance in acquiring the data used in the paper.

References

[1] Muntener M, Patriciu A, Petrisor D, Mazilu D, Bagga H, Kavoussi L, et al. Magnetic resonance imaging compatible robotic system for fully automated brachytherapy seed placement. Urology 2006;68(6):1313–7.
[2] Schmidt MA, Payne GS. Radiotherapy planning using MRI. Phys Med Biol 2015;60(22):R323.
[3] Houdek PV, Schwade JG, Medina AJ, Poole CA, Olsen KR, Nicholson DH, et al. MR technique for localization and verification procedures in episcleral brachytherapy. Int J Radiat Oncol Biol Phys 1989;17(5):1111–4.
[4] McShan D, Ten Haken R, Fraass B. 3-D treatment planning: IV. Integrated brachytherapy planning. The use of computers in radiation therapy. North Holland: Elsevier Science Publishers BV; 1987. p. 249–52.
[5] Kyuma Y, Hayashi A, Odakiri K, Nakamae H. Basic study on MRI guided stereotaxic surgery. Neurol Surg 1989;17(5):449–55.
[6] Schenck JF. The role of magnetic susceptibility in magnetic resonance imaging: MRI magnetic compatibility of the first and second kinds. Med Phys 1996;23(6):815–50.
[7] Ladd ME, Erhart P, Debatin JF, Romanowski BJ, Boesiger P, McKinnon GC. Biopsy needle susceptibility artifacts. Magn Reson Med 1996;36(4):646–51.
[8] Glowinski A, Adam G, Bucker A, van Vaals J, Gunther R. A perspective on needle artifacts in MRI: an electromagnetic model for experimentally separating susceptibility effects. IEEE Trans Med Imaging 2000;19(12):1248–52.
[9] Whitehead G, Ji J. Positive contrast MRI of prostate brachytherapy seeds based on resonant frequency offset mapping. Engineering in medicine and biology society (EMBC), 2010 annual international conference of the IEEE. IEEE; 2010. p. 6641–4.
[10] Ménard C, Susil RC, Choyke P, Gustafson GS, Kammerer W, Ning H, et al. MRI-guided HDR prostate brachytherapy in standard 1.5 t scanner. Int J Radiat Oncol Biol Phys 2004;59(5):1414–23.
[11] Moerland MA, Wijrdeman HK, Beersma R, Bakker C, Battermann JJ. Evaluation of permanent i-125 prostate implants using radiography and magnetic resonance imaging. Int J Radiat Oncol Biol Phys 1997;37(4):927–33.
[12] Shi C, Xie G, Zhang Y, Zhang X, Chen M, Su S, et al. Accelerated susceptibility-based positive contrast imaging of MR compatible metallic devices based on modified fast spin echo sequences. Phys Med Biol 2017;62(7):2505.
[13] Dong Y, Chang Z, Xie G, Whitehead G, Ji JX. Susceptibility-based positive contrast MRI of brachytherapy seeds. Magn Reson Med 2015;74(3):716–26.
[14] Nosrati R, Soliman A, Safigholi H, Hashemi M, Wronski M, Morton G, Pejović-Milić A, Stanisz G, Song WY. MRI-based automated detection of implanted low dose rate (LDR) brachytherapy seeds using quantitative susceptibility mapping (QSM) and unsupervised machine learning (ML). Radiother. Oncol. 2018;129(3):540–7.
[15] Seevinck PR, de Leeuw H, Bos C, Bakker CJ. Highly localized positive contrast of small paramagnetic objects using 3d center-out radial sampling with off-resonance reception. Magn Reson Med 2011;65(1):146–56.
[16] Deshmane A, Gulani V, Griswold MA, Seiberlich N. Parallel MR imaging. J Magn Reson Imaging 2012;36(1):55–72.
[17] Candès EJ, Wakin MB. An introduction to compressive sampling. IEEE Signal Process Mag 2008;25(2):21–30.
[18] Donoho DL. Compressed sensing. IEEE Trans Inf Theory 2006;52(4):1289–306.
[19] Lustig M, Donoho DL, Santos JM, Pauly JM. Compressed sensing MRI. IEEE Signal Process Mag 2008;25(2):72–82.
[20] Lustig M, Donoho D, Pauly JM. Sparse MRI: the application of compressed sensing for rapid MR imaging. Magn Reson Med 2007;58(6):1182–95.
[21] Ullah I, Inam O, Aslam I, Omer H. Accelerating parallel magnetic resonance imaging using p-thresholding based compressed-sensing. Appl Magn Reson 2018:1–19.
[22] Pruessmann KP, Weiger M, Scheidegger MB, Boesiger P. SENSE: sensitivity encoding for fast MRI. Magn Reson Med 1999;42(5):952–62.
[23] Griswold MA, Jakob PM, Heidemann RM, Nittka M, Jellus V, Wang J, et al. Generalized autocalibrating partially parallel acquisitions (GRAPPA). Magn Reson Med 2002;47(6):1202–10.
[24] Jakob PM, Grisowld MA, Edelman RR, Sodickson DK. AUTO-SMASH: a self-calibrating technique for SMASH imaging. Magn Reson Mater Phys Biol Med 1998;7(1):42–54.
[25] Sodickson DK, Manning WJ. Simultaneous acquisition of spatial harmonics (SMASH): fast imaging with radiofrequency coil arrays. Magn Reson Med 1997;38(4):591–603.
[26] King K. Combining compressed sensing and parallel imaging. Proceedings of the 16th annual meeting of ISMRM, Toronto. 1488. 2008.
[27] Wu B, Millane R, Watts R, Bones P. Applying compressed sensing in parallel MRI. Proceedings of the 16th annual meeting of ISMRM, Toronto. 1480. 2008.
[28] Zhao C, Lang T, Ji J. Compressed sensing parallel imaging. Proceedings of the 16th annual meeting of ISMRM, Toronto. 1478. 2008.
[29] Marinelli L, Hardy C, Blezek D. MRI with accelerated multi-coil compressed sensing. Proc. ISMRM 16th scientific sessions. 2008. p. 1484.
[30] Liu B, Sebert F, Zou Y, Ying L. SparseSENSE: randomly-sampled parallel imaging using compressed sensing. In: Proceedings of the 16th annual meeting of ISMRM. 2008.
[31] Liang D, Liu B, Wang J, Ying L. Accelerating SENSE using compressed sensing. Magn Reson Med 2009;62(6):1574–84.
[32] Uecker M, Block K, Frahm J. Nonlinear inversion with l1-wavelet regularization–application to autocalibrated parallel imaging. Proc. Intl. Soc. Mag. Reson. Med. vol. 16. 2008. p. 1479.
[33] Wang Z, Wang J, Detre JA. Improved data reconstruction method for GRAPPA. Magn Reson Med 2005;54(3):738–42.
[34] Vafay Eslahi S, Dhulipala PV, Shi C, Xie G, Ji JX. Parallel compressive sensing in a hybrid space: application in interventional mri. Engineering in medicine and biology society (EMBC), 39th annual international conference of the IEEE. 2017. p. 3260–3.
[35] Vafay Eslahi S, Shi C, Wang H, Ye Y, Chen H, Xie G, et al. Accelerated imaging for visualizing interventional devices using parallel acquisition and compressed sensing reconstruction. Paris, France: *ISMRM*; 2018. p. 1477.
[36] Osher S, Burger M, Goldfarb D, Xu J, Yin W. An iterative regularization method for total variation-based image restoration. Multiscale Model Simul 2005;4(2):460–89.
[37] Chang C-H, Yu X, Ji JX. Compressed sensing MRI reconstruction from 3d multichannel data using GPUs. Magn Reson Med 2017;78(6):2265–74.
[38] Liu J, Liu T, de Rochefort L, Ledoux J, Khalidov I, Chen W, et al. Morphology enabled dipole inversion for quantitative susceptibility mapping using structural consistency between the magnitude image and the susceptibility map. Neuroimage 2012;59(3):2560–8.
[39] Liu T, Liu J, De Rochefort L, Spincemaille P, Khalidov I, Ledoux JR, et al. Morphology enabled dipole inversion (MEDI) from a single-angle acquisition: comparison with cosmos in human brain imaging. Magn Reson Med 2011;66(3):777–83.
[40] Li J, Chang S, Liu T, Wang Q, Cui D, Chen X, et al. Reducing the object orientation dependence of susceptibility effects in gradient echo MRI through quantitative susceptibility mapping. Magn Reson Med 2012;68(5):1563–9.
[41] Ji JX, Son JB, Rane SD. PULSAR: a Matlab toolbox for parallel magnetic resonance imaging using array coils and multiple channel receivers. Concepts Magn Reson Part B Magn Reson Eng 2007;31(1):24–36.
[42] Feng S, Zhu Y, Ji J. Efficient large-array k-domain parallel MRI using channel-by-channel array reduction. Magn Reson Imaging 2011;29(2):209–15.